

Observation and Characterization of Radar Backscatter Over Greenland

Ivan S. Ashcraft, *Member, IEEE*, and David G. Long, *Senior Member, IEEE*

Abstract—Characterization of the microwave signature of the Greenland snow surface enables delineation of the different snow facies and is a tool for tracking the effects of climate change. A new empirical observation model is introduced that uses a limited number of parameters to characterize the snow surface based on the dependence of radar backscatter on incidence angle, azimuth angle, spatial gradient, and temporal rate of change. The individual model parameters are discussed in depth with examples using data from the NASA Scatterometer (NSCAT) and from the C-band European Remote Sensing satellite (ERS) Advanced Microwave Instrument in scatterometer mode. The contribution of each model term to the overall accuracy of the model is evaluated. The relative contributions of the modeled dependencies vary by region. Two studies illustrating applications of the model are included. First, interannual changes over the Greenland ice sheet are investigated using nine years of ERS data. Surface changes are observed as anomalies in the σ° model parameters. Second, intra-annual variations of the surface are investigated. These changes are observed in the average backscatter normalized to a given observation geometry. The results indicate that the model can be used to obtain a more complete understanding of multiyear change and to obtain low-variance high temporal resolution observations of intra-annual changes. The model may be applied for increased accuracy in scatterometer, synthetic aperture radar (SAR), and wide-angle SAR studies.

Index Terms—Empirical model, European Remote Sensing satellite (ERS), Greenland ice sheet, NASA Scatterometer (NSCAT), scatterometer.

I. INTRODUCTION

THE GREENLAND ice sheet plays an important role in the effects of global climate change. Mass-balance of the ice sheet is one of the greatest uncertainties in predicting future sea-level change [1]. Because of the size of the ice sheet and the harsh environment, *in situ* measurements are difficult to obtain, especially on a large scale at frequent intervals. The practical alternative is remote sensing. Spaceborne microwave scatterometers measure the normalized radar cross-section (σ°) over most, if not all, of the ice sheet daily. These measurements do not require solar illumination and penetrate cloud cover making possible consistent temporal and spatial coverage. Additionally, σ° is sensitive to snow grain size, wetness, and subsurface features making possible the mapping of Greenland ice facies [2], the tracking of accumulation [3]–[5], and the measurement of melt extent and duration [6], [7].

Manuscript received May 19, 2004; revised November 17, 2004. This work was supported by the National Aeronautics and Space Administration.

The authors are with the Brigham Young University Microwave Earth Remote Sensing Laboratory, Provo, UT 84602 USA (e-mail: ashcrafti@byui.edu; long@ee.byu.edu).

Digital Object Identifier 10.1109/TGRS.2004.841484

Each scatterometer σ° measurement has a given set of observation parameters including location (typically the measurement centroid) and look geometry (incidence and azimuth angle). Combined, we term these parameters the observation geometry. A perturbation of any of the observation geometry parameters results in a corresponding change in σ° . How σ° changes with the observation geometry is termed the microwave signature of the snow. Temporal trends in the variation of σ° are also part of the microwave signature. The regular and complete coverage of the ice sheet by scatterometers with measurements of σ° at multiple incidence and azimuth angles enables the estimation of the σ° signature of the surface. Our objective is to use scatterometer measurements of σ° to estimate this signature using a small number of model parameters. A simple empirical observation model aids in the observation of σ° and the study of its relationship to the large-scale geophysical properties of the snow.

The σ° signature of the surface is important in at least three ways. First, the parameters characterizing the signature provide a reference frame for monitoring and understanding changes occurring on the surface relating to global climate change and other phenomenon. Changes in the snow surface are observed by a scatterometer as changes in the microwave signature. By closely monitoring the microwave signature and how it varies over time, the temporal variability of the physical properties of the ice sheet can be estimated. Second, an accurate descriptive model of the microwave signature enables the inference of variations from the average microwave signature on relatively short time scales. Using the model, individual measurements can be normalized to a given observation geometry and then compared, making it possible to observe changes at the temporal sampling rate of the sensor, while mitigating the σ° changes due to variations in the observation geometry. Third, the σ° signature is valuable for accurate studies of datasets with limited sampling over the observation geometry. A primary example is the azimuth sampling for synthetic aperture radar (SAR), which is effectively a single azimuth instrument. High-resolution maps of temporal change may be obtained by intercomparing swaths from different time periods. If these passes occur at different azimuth angles, the unaccounted-for differences in σ° due to azimuth modulation may be misinterpreted as being caused by temporal change of the surface. Additionally, processing of wide-angle SAR may be refined by including prior estimates of the azimuth dependence of σ° along the swath.

In this paper, we present a new empirical model for parameterization of the σ° signature over ice sheets. The model is discussed in detail, outlining the theory as well as the relative importance of each individual element. We show the variation of each model parameter across the ice sheet and discuss the phys-

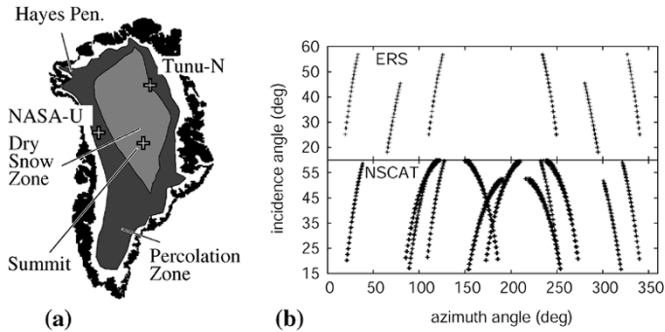


Fig. 1. (a) Locations of key study points used and Benson's ice facies [8] on Greenland. The area outside the ice sheet is black. (b) Scatter-plot of azimuth angle versus incidence angle for ERS and NSCAT at NASA-U during the six months centered around January 1, 1997.

ical interpretation. Two applications of the model are considered: monitoring interannual changes across the Greenland ice sheet by observing the changes in the model parameters over time, and monitoring intraannual change by observing the variation in σ° measurements when normalized to a specific observation geometry using the long-term average σ° signature. Finally, we provide a summary and conclusions. It is anticipated that this model and its variations will be an asset to future studies of Greenland as well as other land/ice studies.

II. BACKGROUND

This study employs data from the C-band European Remote Sensing (ERS) Advanced Microwave Instrument (AMI) in wind scatterometer mode (hereafter referred to as simply ERS) and the Ku-band NASA Scatterometer (NSCAT). Both instruments have a fan beam design with ERS being a single-swath instrument and NSCAT having a dual swath. The fan-beam design provides measurements at a range of incidence angles spanning 20° to 60° from nadir. ERS has three fixed antennas, each measuring vertical polarization σ° at a different azimuth angle. Combining ascending and descending passes provides azimuth sampling at approximately six distinct azimuth angles. NSCAT measures vertical polarization σ° using six antennas that provide azimuth sampling at more angles. Plots of the incidence/azimuth angle sampling for ERS and NSCAT are shown in Fig. 1(b). ERS measurements at all six azimuth angles only occur within the incidence angle range of 25° to 45° . Because of this, only data within the 25° to 45° incidence angle range are included in this study. The same incidence angle range is used for NSCAT to make the study self-consistent. This study primarily uses data from the six month interval from Julian Day (JD) 275, 1996 to JD 90, 1997, which is during the winter months when backscatter from the Greenland surface is relatively constant.

Two locations are used for in-depth analysis throughout this study. These are the Tunu-N (78.0° N, 34.0° W) and NASA-U (73.83° N, 49.5° W) sites. The locations are shown in Fig. 1(a). For each site, Automatic Weather Station (AWS), data are available through the Greenland Climate Network [9]. The raw data analyzed at each location comprise all σ° measurements with centroids that lie within a 25-km radius of the location center.

In addition to focusing on the microwave signature at these two locations, we also present images of the model parameters across the ice sheet. The imaging grid is based on approximately

$8.9 \text{ km} \times 8.9 \text{ km}$ pixels. The σ° model parameter values for each grid element are estimated using least square fit of the model to data within a 25-km radius of the pixel center, identical to the model parameter estimation at the study sites mentioned above. The ice sheet mask is the same as that used by [10], which originated from the Quaternary Map of Greenland produced by the Geological Survey of Greenland.

A basic understanding of the characteristics of the Greenland ice sheet is fundamental to the study of azimuth modulation. Greenland is almost completely covered by a thick layer of snow and ice. Near the summit, this snow layer is over 3 km deep. Because the snow is so deep, ground features are almost entirely masked out leaving a snow surface that is void of mountainous terrain. Mountains are present only on the periphery of the ice sheet near the coast.

Benson [8] divides the Greenland ice sheet into four basic zones or facies. These are illustrated in Fig. 1(a). Melting never occurs in the dry snow zone, which is at the highest altitudes. Below the upper melt line is the percolation zone, where some amount of melt occurs, but the snow-pack does not become saturated. Snow grains in the percolation facies firm are larger than in the dry snow zone due to sublimation associated with melt [8]. Further down slope is the wet or soaked facies where the previous year's accumulation becomes saturated with water during the summer melt. On the periphery of Greenland is the ablation zone where the previous years accumulation completely melts each summer leaving a surface of bare ice and rock. The location of these facies can be estimated from backscatter, which is discussed in Section III-A.

III. OBSERVATION MODEL

In order to parameterize the σ° signature of the Greenland surface, we introduce an empirical observation model

$$\sigma^\circ = A + f(\theta - \theta_{\text{ref}}) + q(\phi) + h(\mathbf{r}) + p(t - t_0) \quad (1)$$

where the variables describing the observation geometry are as follows:

- θ measurement incidence angle;
- θ_{ref} reference incidence angle;
- ϕ measurement azimuth angle;
- \mathbf{r} spatial displacement vector;
- t measurement time;
- t_0 reference time;

and σ° is in decibels. The functions $f(\theta - \theta_{\text{ref}})$, $q(\phi)$, $h(\mathbf{r})$, and $p(t - t_0)$ give the microwave signature relative to the argument parameters. Each is discussed in detail in the following sections. A represents the average at the incidence angle θ_{ref} at time t_0 . We set $\theta_{\text{ref}} = 40^\circ$ and t_0 to the center time of the dataset.

The primary metric used to evaluate the performance of different model formulations is the root mean square (RMS) modeling error

$$\chi = \left(\frac{1}{N} \sum_{i=1}^N (\sigma_i^\circ - \hat{\sigma}_i^\circ)^2 \right)^{(1/2)} \quad (2)$$

where σ_i° is the i th measurement in decibels, and $\hat{\sigma}_i^\circ$ is the corresponding estimate given by (1). To evaluate the model per-

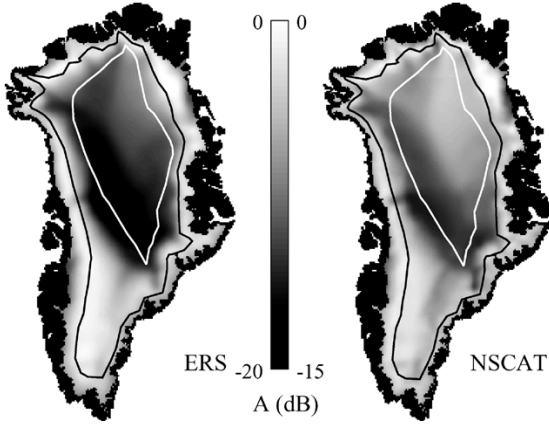


Fig. 2. Images of A (decibels) from NSCAT (Ku-band) and ERS (C-band) estimated using six months of data centered at January 1, 1997. The black and white lines repeat Benson's facies lines from Fig. 1.

formance across the entire ice sheet, we use the average RMS modeling error

$$\bar{\chi} = \frac{1}{M} \sum_{i=1}^M \chi_i$$

where M is the number of imaging pixels within the ice sheet. Using the fully developed model, $\bar{\chi} = 0.375$ dB for ERS, and $\bar{\chi} = 0.458$ dB for NSCAT.

A. Average Backscatter

We first discuss A , which represents the average backscatter normalized to θ_{ref} and t_0 . A key application of A is in delineating the Greenland ice facies [2], [11]–[14]. Images showing the variation in A across the ice sheet for both ERS and NSCAT are shown in Fig. 2. Overlaid on these images are Benson's dry snow and percolation lines. Improved locations for the extent of each of the snow facies can be estimated from microwave data, e.g., [2], [11], and [13]. The dry snow zone is characterized by low A values throughout the center of Greenland. Because the snow grains of dry snow are relatively small, the microwaves penetrate deep in the snow and are absorbed, producing little backscatter.

There is a strong spatial gradient in the backscatter between the dry snow zone and the central percolation zone. At the upper edge of the percolation zone, the summer melt is short and the difference in backscatter from the dry snow zone is relatively small. The short melt results in a crust of *iced firn*¹ on the surface and an increase in snow-grain size due to sublimation [8]. An increase in grain size produces a corresponding increase in A in frozen snow [2]. Further downslope in the percolation zone, the summer melt contributes to the formation of subsurface ice structures termed ice pipes and ice lenses, which form when percolation channels in the wet snow freeze [2]. Surface scattering from the rough tops of the ice lenses and refrozen melt surface causes the bright return in the lower portions of the percolation zone [11], [13].

Downslope from the percolation zone on the edge of the ice sheet is a narrow region of intermediate A values indicating the

¹Iced firn is formed when water-saturated snow freezes.

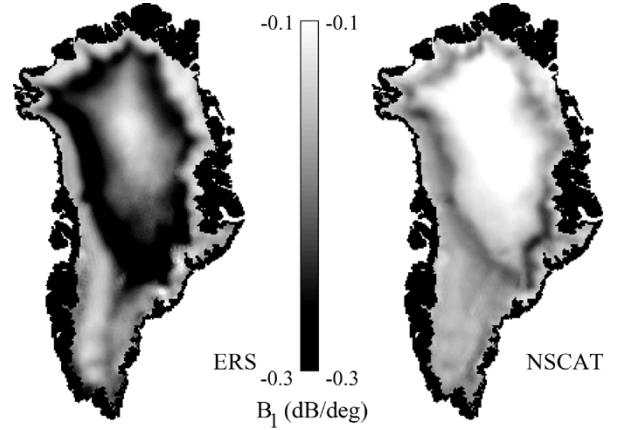


Fig. 3. Images of B_1 from NSCAT and ERS estimated using six months of data centered at January 1, 1997.

wet snow zone [11]. The delineation between the percolation zone and the wet snow zone is perhaps the most difficult to infer using the A images alone because of the low contrast between the two regions. Other parameters perform better for this purpose.

Differences between the ERS and NSCAT A images are also beneficial in delineating the snow facies. Drinkwater *et al.* [4] use this difference to determine the line separating the dry snow and percolation zones. The ERS/NSCAT difference is attributed to the difference in the radar cross-section of the individual snow grains and the penetration depth at the two frequencies. Based on Rayleigh scattering, the radar cross-section of an individual snow grain at higher frequencies (NSCAT) is larger than at lower frequencies (ERS). Accurate quantification of this difference is difficult due to the density of the snow-pack and multiple reflections [15]. The larger σ° values for NSCAT in the dry snow zone are attributed to the difference in the cross-section of the individual snow grains. In the percolation zone, the backscatter is dominated by scattering from subsurface ice structures [13]. At higher frequencies, the penetration depth is reduced in snow, leading to increased attenuation between the snow surface and the subsurface ice layers/structures. The smaller σ° values for NSCAT compared to ERS in the percolation zone are attributed to this penetration depth effect.

B. Incidence Angle Dependence

In our model, σ° varies as a quadratic function of incidence angle where σ° is in decibels, and θ is in degrees, i.e.,

$$f(\tilde{\theta}) = B_1 \tilde{\theta} + B_2 \tilde{\theta}^2 \quad (3)$$

where $\tilde{\theta} = \theta - \theta_{\text{ref}}$. The B_1 term indicates the magnitude of the linear dependence of σ° on incidence angle [2], [4]. B_2 indicates the magnitude of the quadratic dependence of the backscatter on incidence angle. B_2 has been assumed to be negligible in previous studies over Greenland. Any constant offset is subsumed into A . In this study, the incidence angle has not been adjusted for the large-scale surface slope. This affects the azimuth dependence of σ° and is discussed in the next section.

The B_1 images in Fig. 3 show to what degree the linear incidence angle dependence of σ° varies across the ice sheet. In general, B_1 is an indicator of the contribution of volume scattering versus surface scattering. An increase in the magnitude

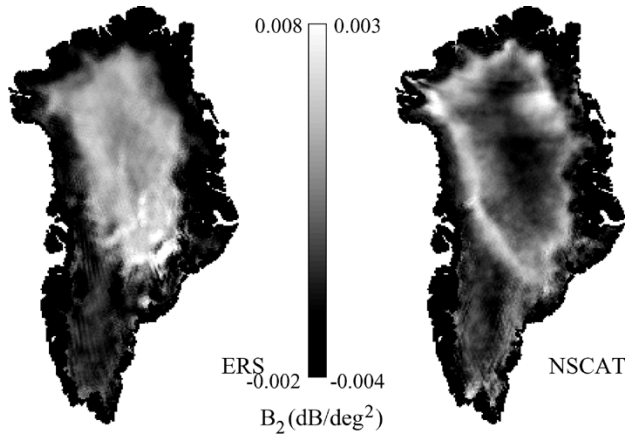


Fig. 4. Images of B_2 from NSCAT and ERS estimated using six months of data centered at January 1, 1997.

of B_1 indicates a greater contribution from surface scattering. Based on this premise, some general conclusions are obtained from the B_1 images.

For ERS, $|B_1| \approx 0.3$ dB/degree in the upper percolation zone, which is nearly double that observed across the rest of the ice sheet, suggesting that in the upper percolation zone the relative contribution from surface scattering is much larger than elsewhere. This is attributed to the iced firm forming on the surface after a melt event [8] contributing to increased surface scattering. The key difference between the upper and lower percolation zone is that in the lower percolation zone the longer melt results in the formation of subsurface ice structures that contribute to the increased volume-like scattering. Similarly, for NSCAT, the largest B_1 magnitude is observed in the dry snow zone, indicating increased relative contribution from surface scattering in this area.

A key difference between the NSCAT and ERS estimates of B_1 is observed in the dry snow zone. The smaller magnitude of B_1 for NSCAT suggests that the relative contribution from volume scattering is much more significant in this region at Ku-band. This difference between C-band and Ku-band is attributed to volume scattering in the dry snow zone originating primarily from the individual snow grains. The grains are electrically larger at Ku-band, corresponding to larger individual radar cross-sections. This is consistent with the larger A values observed for Ku-band in the dry snow zone. The ERS and NSCAT B_1 are similar in the lower percolation zone and wet snow zone where the volume-like scattering is attributed to subsurface ice structures that are electrically large at both C-band and Ku-band. Variations of B_1 within the dry snow zone are attributed to the variation in the accumulation rate where more negative B_1 values indicate regions of higher accumulation [4].

Fig. 4 shows how B_2 (the quadratic dependence on incidence angle) varies across the ice sheet. For our dataset, which includes the incidence angle range from 25° to 45° , B_2 is an indicator of the relative contribution of surface scattering at low incidence angles.

For ERS, the B_2 values are most positive in the dry snow zone and upper percolation zone, indicating that the relative contribution of surface scattering at low incidence angles is largest

in these areas. For NSCAT, the most positive B_2 values are observed in the upper percolation zone. The large B_2 values in the upper percolation zone are attributed to the large relative contribution of surface scattering to the overall backscatter in this region. In the dry snow zone, the difference in B_2 between the two frequencies is attributed to surface scattering contributing relatively more to the overall backscatter for ERS than for NSCAT. This reasoning is consistent with the observations from the B_1 images.

The modeling of incidence angle dependence is critical to the model. Without incidence angle dependence in the model, the average RMS modeling error is $\bar{\chi} = 1.26$ dB for ERS and $\bar{\chi} = 0.957$ dB for NSCAT. This is an increase of 220% and 109%, respectively, relative to using the full model. Including linear incidence angle dependence reduces the modeling error to $\bar{\chi} = 0.393$ dB for ERS and $\bar{\chi} = 0.461$ dB for NSCAT (4.8% and 0.66% larger, respectively, than obtained using the full model, which includes the second-order B_2 term).

C. Azimuth Angle Dependence

The signature of σ° with azimuth angle provides valuable information relating to the surface profile. Wind-formed erosional snow features known as sastrugi are a dominant factor driving azimuth modulation [16]. Sastrugi crests are parallel to the wind direction [17], resulting in local minima in the azimuth modulation in the up/down wind directions and a local maximum in the cross-wind directions. Data fits to the observation model presented in this paper yield results consistent with this theory.

Using a simple physical model, we [18] find that azimuth dependence of σ° can be directly related to aeolian-formed surface features such as sastrugi, i.e., the physical model indicates that azimuth modulation of σ° over Greenland is related to katabatic wind flow, which is similar to findings over Antarctica [16], [17], [19], [20]. Using a physical model provides valuable insights into the relationship between surface features and backscatter; however, inversion of the model requires second-order iterative nonlinear regression. To enable faster, more robust model inversion, we adopt an empirical linear descriptive model that provides accuracy similar to the physical model. This empirical model facilitates the data normalization with respect to azimuth angle, which is essential for accurate intermeasurement comparisons.

Our model for the variation of σ° with azimuth angle consists of the second-order Fourier Series

$$q(\phi) = M_1 \cos(\phi - \phi_1) + M_2 \cos(2\phi - \phi_2) \quad (4)$$

where M_1 and M_2 are the magnitudes of the first- and second-order azimuth modulation respectively, and ϕ_1 and ϕ_2 are the orientations. This empirical model is chosen because it minimizes the model complexity and accurately exhibits the properties of the data. This simple empirical model is also appropriate for the scale: it requires a minimal amount of knowledge of the geophysical properties of the surface, which may vary widely across the scatterometer footprint and within the penetration depth of the radar. Additionally, this is a simple diagnostic model that is suitable for identifying the sensitivity of σ° to azimuth variation.

Our azimuth dependence model is similar to models used previously for the azimuth signature of σ° over Antarctica, which has an environment similar to Greenland. The models previously proposed for the azimuth signature over Antarctica each include one or more terms of a Fourier Series. Ledroit *et al.* [19] use a bisinusoid based on a theoretical model of ocean backscatter to model azimuth dependence of Seasat-A scatterometer measurements over Antarctica, finding azimuth dependencies as large as 5 dB at Ku-band. Similarly, Young *et al.* [20] use a bisinusoid to model ERS variations over Antarctica, finding azimuth modulations of similar magnitude (5.5 dB peak-to-peak maximum) for C-band. Long and Drinkwater [16] added a first-order sinusoid for their analysis and linear variation in the magnitude of the modulation with incidence angle. The net finding of these studies is that azimuth modulation over Antarctica is primarily second order (180° symmetry), and its orientation is related to the prevalent surface wind direction.

Because azimuth dependence of σ° over Greenland has not previously been investigated in depth, we devote considerable effort to this topic. First, we explore the azimuth dependency of the data relative to the azimuth variation in the model. Next, we briefly discuss the relationship between azimuth dependence and wind flow, showing estimated wind flow maps based on the σ° signature of the surface for both ERS and NSCAT. Subsequently, we use nine years of ERS data for analysis of the long-term variability in the azimuth signature of σ° . Finally, we briefly investigate how the azimuth signature varies with incidence angle and find this variation to be relatively insignificant given the inherent variance of the data.

To illustrate the fit of the second-order Fourier Series to ERS and NSCAT data, we use measurements from the NASA-U and Tunu-N sites discussed in Section II. The model fit to the data is shown in Fig. 5. The plots show the model estimate of the azimuth modulation, $q(\phi)$ [see (4)], versus the raw data with the dc bias and all dependencies besides azimuth removed, i.e.,

$$q_i = \sigma_i^\circ - A - B_1(\theta_i - \theta_{\text{ref}}) - s_1(\mathbf{r}_i \cdot \mathbf{g}). \quad (5)$$

As observed in Fig. 5, a second-order fit is required to adequately describe the azimuth dependence. At NASA-U and Tunu-N, a local minimum of the ERS and NSCAT backscatter with azimuth angle matches the measured dominant wind direction as illustrated in Fig. 5. These results are consistent with the idea that sastrugi are a dominant factor contributing to azimuth modulation.

Images of the model parameters related to azimuth dependence are shown in Fig. 6. The M_1 and M_2 images show estimates of the magnitude of the azimuth anisotropy of the σ° measurements. Fig. 6 suggests that the azimuth dependence (both M_1 and M_2) is generally larger for ERS than for NSCAT (note the difference in the scales—compare also Fig. 5). For both instruments, the dependence is primarily second order, indicative of 180° symmetry in the microwave properties of the firn. Although smaller, the magnitude of the first-order dependence (M_1) is nonnegligible. The first-order azimuth dependence is attributed in part to the large-scale slope of the surface, which is not accounted for in the incidence angle calculation. The slope effectively biases the reported incidence angle relative to

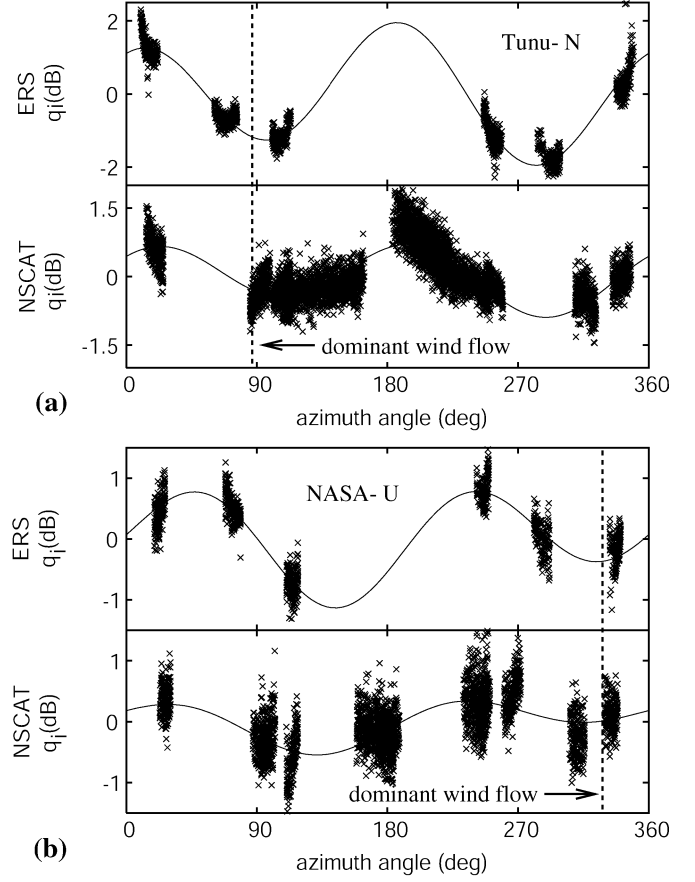


Fig. 5. Azimuth dependency observed in the data using six months of data centered at January 1, 1997 and the model at (a) Tunu-N and (b) NASA-U. Normalized raw data measurements (q_i) are shown as “+” marks, and the line indicates the model estimate ($q(\phi_i)$) of the azimuth dependence. The dominant wind direction during 1996 based on AWS data from the Greenland Climate Network [9] is indicated by a vertical dotted line on each plot. The wind direction coincides with a local minimum of the azimuth modulation, which supports the theoretical correlation between wind direction and azimuth modulation.

the true incidence angle relative to the surface normal. Observations from up-slope are biased high and observations from down-slope are biased low.

The azimuth dependence (both M_1 and M_2) is largest in the lower portions of the dry snow zone and the transition region from the dry snow to percolation zone. The largest azimuth dependence is found in the northeast dry snow zone where the accumulation rate is relatively low [21]. Moving south from the northeast dry snow zone, a decrease in the magnitude of the azimuth dependence is observed. The location of this decrease corresponds to the windward side of a ridge running northeast from the summit. The reduction in the azimuth modulation in this area is attributed to a decrease in the katabatic wind flow due to the wind flowing cross- or up-slope rather than down-slope [18]. There is a general decrease in the azimuth modulation moving from the dry snow zone to the percolation zone, especially with ERS. This is attributed to the scattering from subsurface ice structures, which dominates the backscatter in this region [13] and is wind independent.

Streamlines in the azimuth direction of the backscatter minimum for ERS and NSCAT are shown in Fig. 7(a). The streamlines are imposed over M_2 images from the corresponding sensor. The streamlines can represent an estimate

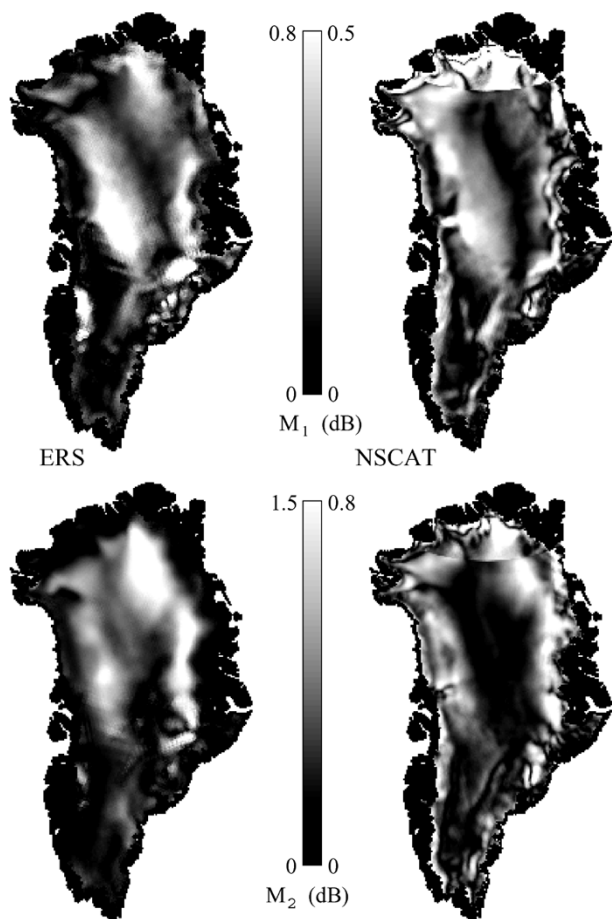


Fig. 6. Images of the magnitude of the azimuth dependence parameters M_1 and M_2 .

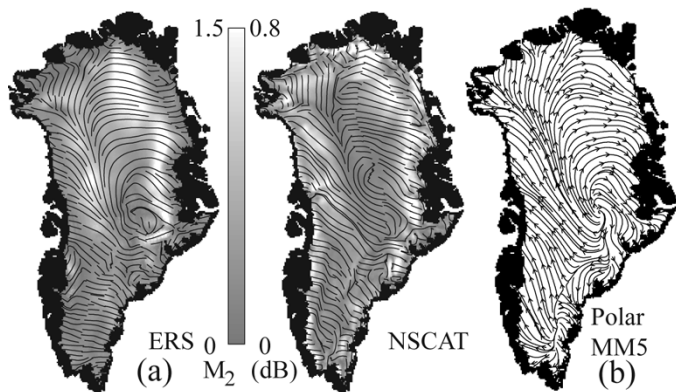


Fig. 7. (a) Streamlines of second-order azimuth modulation minimums for ERS and NSCAT. The streamlines are imposed over M_2 images from the respective sensors. (b) Streamlines of annual mean wind directions for 1991–2000 period based on a Polar MM5 model simulation (adapted from [23]).

of the mean wind flow and are highly correlated with modeled katabatic wind fields [22], [23] [see Fig. 7(b)], with the largest differences between the scatterometer-derived winds and modeled winds occurring in southwest Greenland. A strong feature in the streamline flow is the divergent region progressing northwest from the summit to the Hayes Peninsula. Differences observed between ERS and NSCAT wind estimates

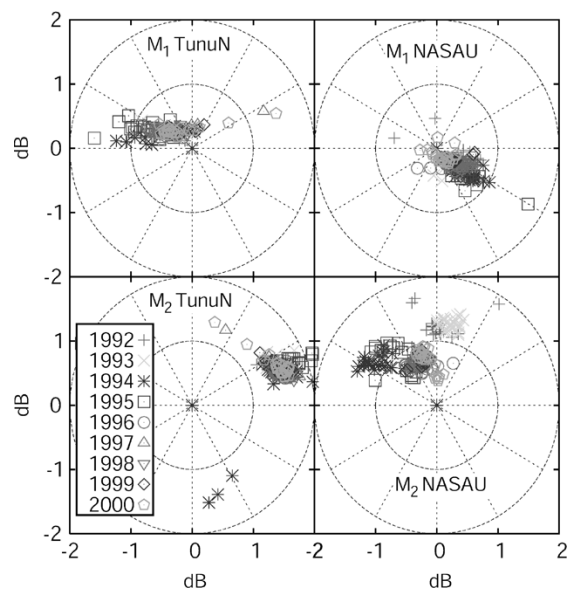


Fig. 8. Scatterplots of the azimuth modulation parameters. Each symbol represents the end point of a vector representation of the magnitude and orientation of the azimuth modulation.

are attributed to Ku-band being sensitive to smaller roughness scales and also having smaller penetration depths than C-band.

The azimuth dependence is deemed an important part of the model based on its contribution to the overall model accuracy. Without modeling azimuth modulation, the model yields $\bar{\chi} = 0.591$ dB for ERS and $\bar{\chi} = 0.550$ dB for NSCAT, 58% and 20% larger respectively than the full model, which includes the M_1 and M_2 terms. Inclusion of only first-order (M_1) modulation reduces the error to $\bar{\chi} = 0.504$ dB for ERS and $\bar{\chi} = 0.511$ dB for NSCAT (34% and 12% larger than the full model). Including only second-order dependence results in smaller errors: $\bar{\chi} = 0.423$ dB for ERS and $\bar{\chi} = 0.491$ dB for NSCAT (12.8% and 7.2% larger than the full model).

1) *Long-Term Stability of Azimuth Modulation:* A question that arises in analyzing the azimuth dependence of σ° is how it varies with time. Over the ocean, the azimuth signature of σ° responds almost immediately to changes in wind direction and speed. Over Greenland, we expect a much slower change in azimuth dependence because the changes in the surface profile with wind change are not as immediate as those over the ocean. Also, the backscatter is a composite of scattering from multiple layers, which effectively makes the azimuth signature dependent upon the wind flow over an extended period of time. The length of time represented depends on the penetration depth, layer thickness, and relative magnitude of the backscatter from the individual layers.

To investigate the rate of change of the azimuth signature, we use parameter estimates from nine years of ERS data with the parameters estimated at 15-day intervals using 30 days of data. The first- and second-order azimuth modulation are viewed as vectors where M_1 and M_2 are the vector magnitudes, and ϕ_1 and ϕ_2 are the vector orientations. To evaluate the temporal variability in the σ° azimuth signature, we observe how these vectors change over time. Examples for the NASA-U and Tunu-N sites are shown in Fig. 8. Each point on the scatterplots indicates a vector endpoint. The vector endpoints are well clustered over

individual years, indicating that the azimuth modulation is relatively stable annually. The few outliers are attributed to ill-conditioned estimations where the sampling of one or more of the basis elements is insufficient over the given time interval.

Some changes in the azimuth modulation are observed from year to year. The largest change is in M_2 at NASA-U between 1993 and 1994. The orientation of M_2 shifts $\sim 40^\circ$. From 1994 to 1996, the orientation appears to slowly move backward $\sim 20^\circ$, and the magnitude decreases by ~ 0.3 dB. This annual change in azimuth modulation appears to be localized to small areas and is discussed further in Section IV-A.

Further investigations across the ice sheet give similar results. Azimuth modulation parameters are consistently well clustered, falling in the same general direction over the nine-year period. We suggest two reasons for the observed long-term stability. First, since the backscatter is a response from multiple buried layers, it represents a long-term average of the annual formation of the surface structure continually buried by additional accumulation. Second, the direction of the average wind flow is relatively steady. Because of its stability over time, the azimuth modulation parameters are useful in monitoring long-term interannual changes that occur in the average wind flow pattern.

2) *Variation in Azimuth Dependence With Incidence Angle:* Another question arising in the analysis of the azimuth signature of σ° is how this signature varies with incidence angle. Ledroit *et al.* [19] state that large-scale roughness corresponds with azimuth modulation at low incidence angles, and small-scale roughness corresponds to azimuth modulation at high incidence angles. Thus, the variation of azimuth modulation with incidence angle is an indication of the relative roughness of the surface features driving the modulation. The model proposed in [16] assumes that M_1 and M_2 vary linearly with incidence angle, i.e.,

$$M_i = c_i + d_i(\theta - 40) \quad (6)$$

where c_i and d_i are constants.

We investigate the dependence of azimuth modulation on incidence angle by plotting the residual errors as defined in (2) versus the basis of the d_i parameters, $b_1 = (\theta - 40) \cos(\phi - \phi_1)$ and $b_2 = (\theta - 40) \cos(2\phi - \phi_2)$ (see Fig. 9). Any dependency of M_1 and M_2 on incidence angle is expected to appear in the plots. The observed dependence is small, approximately ± 0.2 dB, which is significantly smaller than the composite modeling error and noise. This suggests that in the 25° to 45° incidence angle range the dependence of azimuth modulation on incidence angle is relatively insignificant in Greenland. The calculation of the RMS residual errors confirms this, showing negligible improvement when the azimuth modulation magnitude is modeled as a linear function of incidence angle.

D. Spatial Gradient

To account for biases arising from small differences between the measurement center locations and the location for the model estimation, we include a model term which we refer to as the *spatial gradient*. The spatial gradient is defined as the rate of change in the magnitude of the backscatter relative to small changes in geographical location. Prior to our inclusion of the

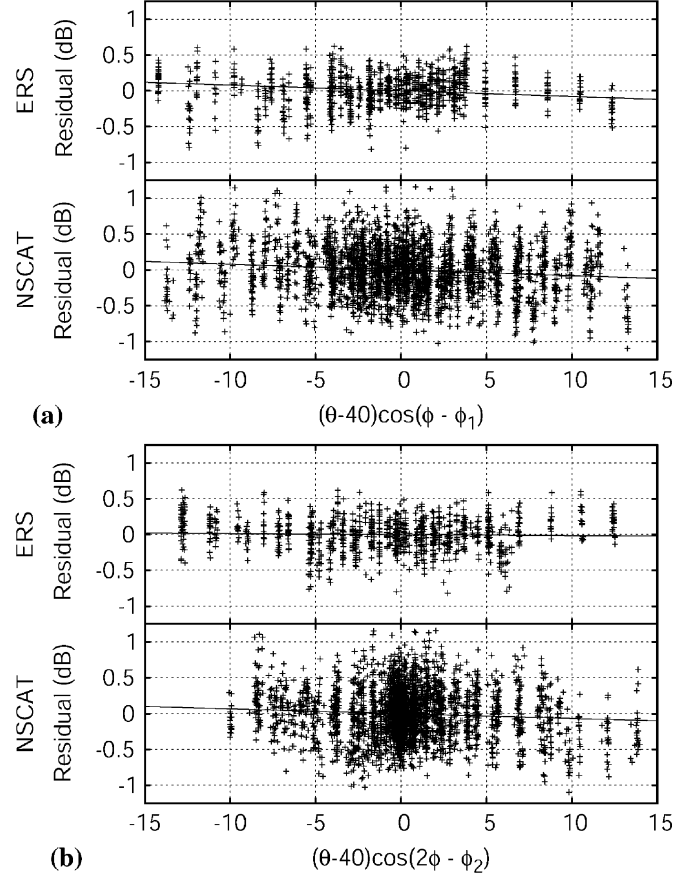


Fig. 9. Plots indicating the incidence angle dependence of the azimuth modulation magnitude at the NASA-U site. The line in each plot shows a linear fit to the data. (a) ERS and NSCAT residual errors versus $(\theta - 40) \cos(\phi - \phi_1)$, which is a basis for incidence angle dependence of the first-order azimuth modulation. (b) ERS and NSCAT residual errors versus $(\theta - 40) \cos(2\phi - \phi_2)$, which is a basis for incidence angle dependence of the second-order azimuth modulation. In all cases, the dependence of the azimuth modulation magnitude on incidence angle is small.

spatial gradient into the model, we found the largest modeling error to be in the the percolation zone, the zone with the largest spatial gradient in backscatter. As discussed in Section II, the dataset for each study location includes σ° measurements that have centroids within a 25-km radius of the study site. The 50-km resolution backscatter may vary significantly within this radius, producing what we term a *colocation* bias in the measurements. In these regions, the colocation bias is significantly reduced by incorporating the spatial gradient into the model. We model the spatial gradient of this dataset using

$$h(\mathbf{r}) = s_1(\mathbf{r} \cdot \hat{\mathbf{g}}) \quad (7)$$

where s_1 is the magnitude of the gradient, $\hat{\mathbf{g}}$ is a unit vector in the direction of the backscatter gradient, and \mathbf{r} is a vector from the center of the study site to the measurement centroid. Estimating the spatial gradient simultaneously with the other model parameters reduces parameter estimation error caused by nonuniform spatial sampling. Also, by including the spatial gradient in the model, the effects of the colocation bias on the modeling error are reduced, increasing the effectiveness of using the modeling error to determine the applicability of the observation model in characterizing the variability of σ° .

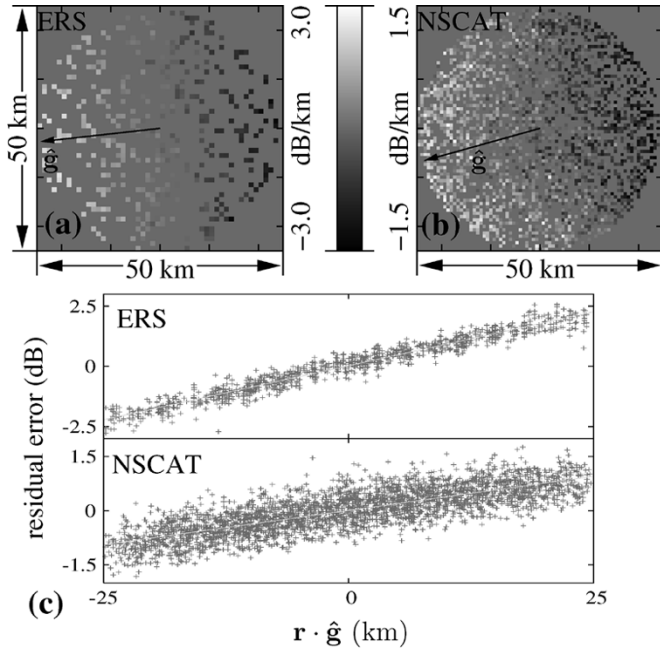


Fig. 10. Colocation bias plots for the NASA-U site. (a) Magnitude of the residual error for ERS versus the displacement of the measurement center from the NASA-U site. The magnitude of the error is indicated by the grayscale. (b) Magnitude of the residual error for NSCAT versus the displacement of the measurement center from the NASA-U site. (c) ERS and NSCAT residual errors versus $r \cdot \hat{g}$, the distance from the center of the study area to the measurement location in the \hat{g} direction.

Fig. 10 shows the dependence of modeling error on \mathbf{r} for ERS and NSCAT data at the NASA-U site for the case where only azimuth and incidence angle dependence are included in the model. The colocation bias is clearly evident in the modeling error. The plots indicate that the colocation bias contributes significantly to the variability of the dataset with a bias of ~ 2.4 dB for ERS and ~ 1.1 dB for NSCAT at 25 km from the location center.

The colocation bias has at least two negative effects on σ° analysis in these regions. First, the model parameter estimation may be corrupted based on the spatial sampling of the dataset due to unmodeled colocation bias. For example, an estimate of B is corrupted if the colocation bias of low incidence angle measurements is negative, and the colocation bias of high incidence angle measurements is positive due to the measurement locations. Second, when the colocation bias is ignored, the modeling error is biased high due to the spatial spread of the measurement centroids and the spatial variability in the backscatter. This limits use of modeling error as a tool to evaluate incidence and azimuth-angle-dependent models.

Images of the magnitude of the spatial gradient (s_1) with streamlines showing the gradient orientation ($\angle \hat{g}$) are shown in Fig. 11. The magnitude of the spatial gradient is largest in the upper percolation zone due to the extreme change in backscatter over this region. In this region, the backscatter varies from some of the lowest σ° values observed over Greenland (near the dry snow zone boundary) to the highest Greenland σ° measurements, which occur in the central percolation zone.

Key differences are observed between the σ° spatial gradient at C-band and Ku-band. First, we observe that the maximum s_1 values, which are located in the upper percolation zone, are smaller at Ku-band than C-band. Second, the orientation of the

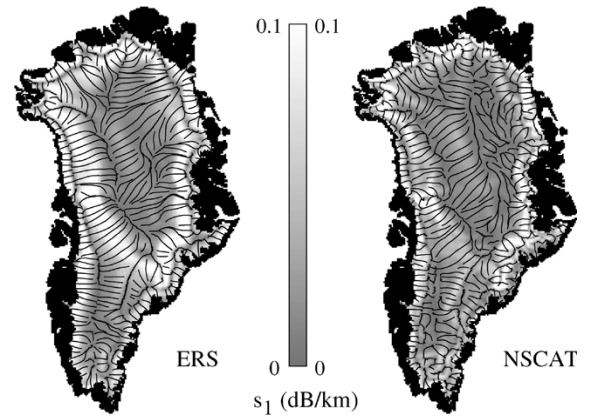


Fig. 11. Images showing the spatial gradient magnitude (s_1) and streamlines showing the orientation of the spatial gradient.

gradient shows some frequency differences. An area of note is in the northeast dry snow zone where at C-band the gradient is nearly east–west, while at Ku-band the gradient is nearer to north–south. One explanation of this phenomenon originates from the difference in the penetration depth between the two sensors. The east–west gradient observed in ERS is attributed to the transition from the dry snow zone to the percolation zone where subsurface ice structures contribute to increased backscatter. However, if this area has not melted significantly over the last few years, the accumulated snow further buries these ice structures and iced firn layers, making them less visible at Ku-band than C-band due to the difference in penetration depths. The gradient for NSCAT is smaller in this region and dominated by properties other than the transition between snow zones such as accumulation rate. A second area of difference in $\angle \hat{g}$ with frequency is the southwest percolation zone. With ERS, a single peak is observed in s_1 based on a single discontinuity observed in $\angle \hat{g}$ in this region. However, for NSCAT there appear to be two separate peaks. This is attributed in part to the higher spatial resolution intrinsic in the NSCAT measurements.

The contribution of the spatial gradient to the overall accuracy of the model is significant. When the spatial gradient is ignored, the RMS modeling error is $\bar{\chi} = 0.737$ dB for ERS and $\bar{\chi} = 0.658$ dB for NSCAT, a relative increase of 97% and 44%, respectively, over the value of $\bar{\chi}$ obtained using the full model.

E. Temporal Dependence

Because we are using data over six months, we expect some migration in the mean backscatter during this period. We model this dependence, $p(t)$ from (1), as a linear function of time over the six-month interval

$$p(t) = Tt. \quad (8)$$

The images of T for ERS and NSCAT are shown in Fig. 12. Two key features are found in these images. First, there is a linear decrease of approximately 1 dB/year over regions of the upper percolation zone. This is attributed to accumulation over a region in the upper percolation zone, which experienced melt during the last summer [3]. The second key feature is ~ 1 dB/year estimated increase in σ° throughout the wet snow zone as observed by ERS. This feature aids in delineating the wet snow zone from the percolation zone, a division weak in the other parameter images.

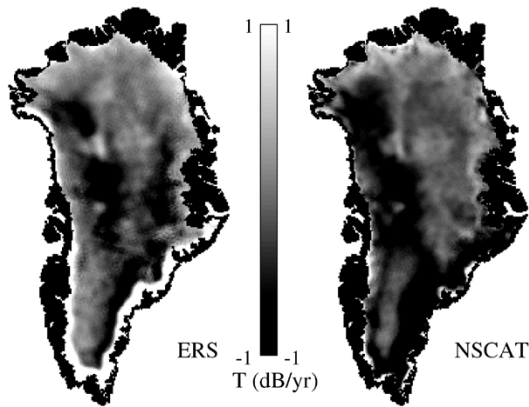


Fig. 12. Images of T for the six months centered around January 1, 1997.

The improvement in the model accuracy gained by including temporal dependence is small but nonnegligible. Without temporal dependence, the modeling error is $\bar{\chi} = 0.401$ dB for ERS and $\bar{\chi} = 0.470$ dB for NSCAT, 6.9% and 2.6% larger, respectively, than the full model.

IV. APPLICATIONS

The descriptive empirical model presented in this paper is applicable for studying both long- and short-term changes over the ice sheet. We present examples of each using ERS data. First, we show interannual changes that indicate regions of significant variation over the nine-year ERS period. Then, we show how the model can be used to study intraannual changes. Compared with previous methods, using the model provides a lower variance signal, increasing the ability to detect small-scale short-term variation as well as increased temporal resolution.

A. Interannual Change

Annual changes in individual parameters indicate important geophysical changes occurring across the ice sheet. Fig. 13 shows images of the anomaly between the estimates of the individual parameters each year and the average for the nine-year period for ERS. The parameter estimates for the individual years are from six months of data during midwinter spanning the years indicated. The anomaly images show changes that have occurred prior to this six month span, commonly occurring the previous summer.

In the A images, the changes observed near the dry snow/percolation transition zone indicate the reach of the melt each summer [3], [24]. The annual anomaly images indicate below-average melt during the summers of 1993, 1994, and 1996. After 1995, increased melt is observed in the west and south. After 1997, high melt is observed in the southern dry snow zone. After 1998, the northeast, and after 1999, the south are focus points indicating increased melt. After 2000, evidence of increased melt is observed in a large area in the west dry snow zone. The net result is an increase in A from the northwest corner of the dry snow zone, down along the west edge to the southern end, and back up the east side. This is consistent with [6] and [25].

The changes observed in the B_1 images are also associated with the annual melt extent/intensity. After 1992, 1993, and

1995, the B_1 values in the central percolation zone are more negative than average. This is indicative of a below-average intensity melt where a reduced volume of subsurface ice structures form. The resulting reduction in volume-like scattering leads to increased relative contribution from surface scattering from layers, causing B_1 to become more negative. This effect is reversed after 1997 and 1998, indicating above average intensity melting. A strong melt event contributes to the formation of subsurface ice structures, increasing volume scattering which causes B_1 to become more positive. After 1999 and 2000, B_1 becomes more negative along the dry snow zone boundary, indicating melt is occurring in areas not affected by melt in recent years. Here, surface scattering increases due to layers of iced firn forming over the previously dry snow. Some artifacts due to variations in the sampling resulting from missing ERS scatterometer data during SAR operations are observed as faint lines in the 1993/1994 and 1995/1996 images.

The M_1 and M_2 images show azimuth modulation variation across the ice sheet. Significant annual changes are observed in small regions of the upper percolation zone as discussed in Section III-C. These are the same regions where large changes in A are attributed to increased melt. The net result is a decrease in the azimuth modulation along the upper western percolation zone. Decreases occur in step increments coinciding with increased melt as observed in the A images. One exception is observed where a below-average summer melt during 1993 appears to contribute to a significant decrease in the azimuth modulation the following winter. Both M_2 and A decrease along the western transition zone. The only significant increase in azimuth modulation occurs in M_2 after the summer of 1994 in the eastern transition zone. This increase is short-lived, almost completely vanishing after the next summer.

The s_1 images are key indicators of the location of the upper percolation zone and of the spatial rate of change in the snow properties progressing outward from the dry snow zone. The gradient is large in the upper portion of the percolation zone and decreases downslope as the snow becomes spatially uniform in the number of subsurface ice structures. From 1992 through 1994, s_1 is lower than average near the dry snow zone boundary, indicating that the true boundary between the dry snow zone and percolation zone is further downslope than average. The opposite is observed after 1997 and into the following years. During these years, s_1 is larger than average, indicating an upslope movement of the percolation zone/dry snow zone boundary.

The T images are an indicator of accumulation rather than melt intensity/extent. In the percolation zone, the more negative values of T correspond to higher rates of accumulation [3], [4]. Each T anomaly image is indicative of the accumulation during the previous year. The T images indicate that 1992/1993, 1995/1996, 1998/1999, and 1999/2000 were winters with above average accumulation and 1993/1994, 1996/1997, and 1997/1998 were winters of lower than average accumulation. These results are consistent with the accumulation estimates of [26]. The reductions in T observed along the western dry snow boundary in the 1996/1997 and 1999/2000 images are attributed to an above-average melt extent the previous summer that results in the linear decrease in σ° associated with accumulation observed in these new melt areas.

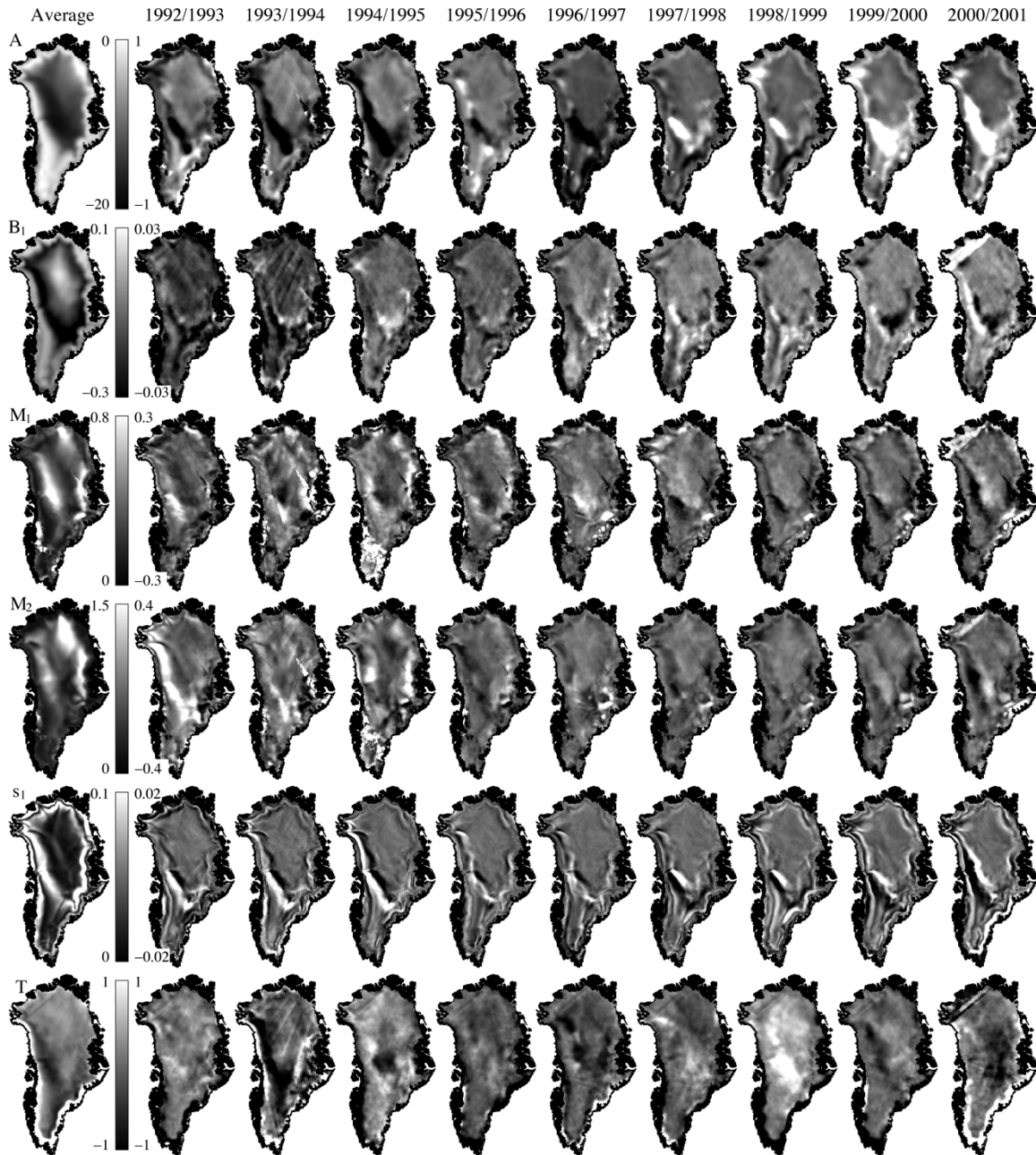


Fig. 13. Images showing (left column) the average model parameter values over nine winters and (columns right of grayscale bar) the annual anomalies (model parameter minus mean).

B. Intraannual Variations

In addition to observing interannual changes across the ice sheet, observations of intraannual trends are critical to understanding the relationship between σ° and geophysical properties of the surface. Our model is applicable for improved analysis of surface variation on short time scales. Because complete characterization of the microwave signature at fine time scales requires more information than is presently available or practical, the application of this model to short time-scale analysis requires some basic assumptions about the microwave signature.

The primary assumption of our method is that for the short time-scale considered, the variability of σ° with the observation geometry is relatively constant, and changes in the surface and subsurface primarily affect the average backscatter. Assuming a

constant geometry signature (CGS) is supported by the previous section. Over most of the ice sheet, the parameters describing the dependence of σ° on the observation geometry are relatively constant over time. The primary location where CGS is questionable is the upper percolation zone where significant annual changes are observed in the model parameters. These changes are attributed to summer melt, making the CGS assumption applicable only during periods between summer melt events.

To develop our methodology for intraannual analysis using the CGS assumption, we begin with the full model given in (1) where the temporal dependent term $p(t)$ is subsumed into $A(t)$, i.e.,

$$\sigma^\circ = A(t) + f(\theta - \theta_{\text{ref}}) + g(\phi) + h(\mathbf{r}). \quad (9)$$

With the CGS assumption, only $A(t)$ in this model varies with time. Thus, $A(t)$ contains all information about the temporal variation of the surface. To estimate $A(t)$, we first estimate the geometry-dependent model parameters using least square estimation based on data over an extended time period. Using the estimated geometry signature, we obtain estimates of $A(t)$ at each measurement time t_i by differencing the measurement (σ_i°) and the observation geometry dependent portion of the model, i.e.,

$$A(t_i) = \sigma_i^\circ - f(\theta_i - \theta_{\text{ref}}) - g(\phi_i) - h(\mathbf{r}_i). \quad (10)$$

The result is an estimate of the variation of the average backscatter over time.

Variations in the average backscatter ($A(t)$) have been used to estimate accumulation [3], [4], monitor melt and ablation [2], [6] and study long-term climate change [27], [28]. Using our model with the CGS assumption enables lower variance estimates of $A(t)$ and increased temporal resolution compared with the methods used in these studies. Without the CGS assumption, the dependence on observation geometry must be reestimated with each estimate of the average backscatter. There are several drawbacks to continually reestimating the dependence of σ° on the observation geometry. First, to enable higher temporal resolution, a simpler model must be used. This results in residuals from unmodeled dependencies increasing the variance in the observation signal. Second, to increase temporal resolution, a relatively small number of data samples are used. This may contribute to poor estimates of the model parameters due to limited sampling in incidence angle and/or other modeled dependencies. Third, even with the simplified model, multiple days of data are typically required to obtain estimates of the average backscatter, significantly limiting the achievable temporal resolution.

Assuming CGS provides significant improvement in each of these areas. Errors in the signal due to observation geometry sampling are mitigated using our more complete descriptive model. Using data from an extended time period increases the number of samples, making the estimation of the dependence on observation geometry much more robust. The best temporal resolution is equal to the temporal sampling of the sensor because each σ° measurement is associated with an estimate $A(t_i)$.

To evaluate the performance using CGS, we examine two examples in which the results using CGS are compared with results assuming variable geometry signature (VGS). For VGS, we use the method from the studies mentioned above. The simplified model for observation geometry dependence is

$$\sigma^\circ(\theta) = A + B(\theta - \theta_{\text{ref}}) \quad (11)$$

which includes incidence angle dependence only. A and B are estimated using linear least squares regression for three days of ERS data within a 25-km radius of the study site. Estimates are made at three-day intervals.

For the CGS method, the full model parameters are estimated using ERS data from the six-month interval including October 1997 through March 1998. The $A(t_i)$ values are averaged over three days so that the two methods are consistent in time sampling. The averaging also reduces the variance of the signal at the cost of lowering the temporal resolution.

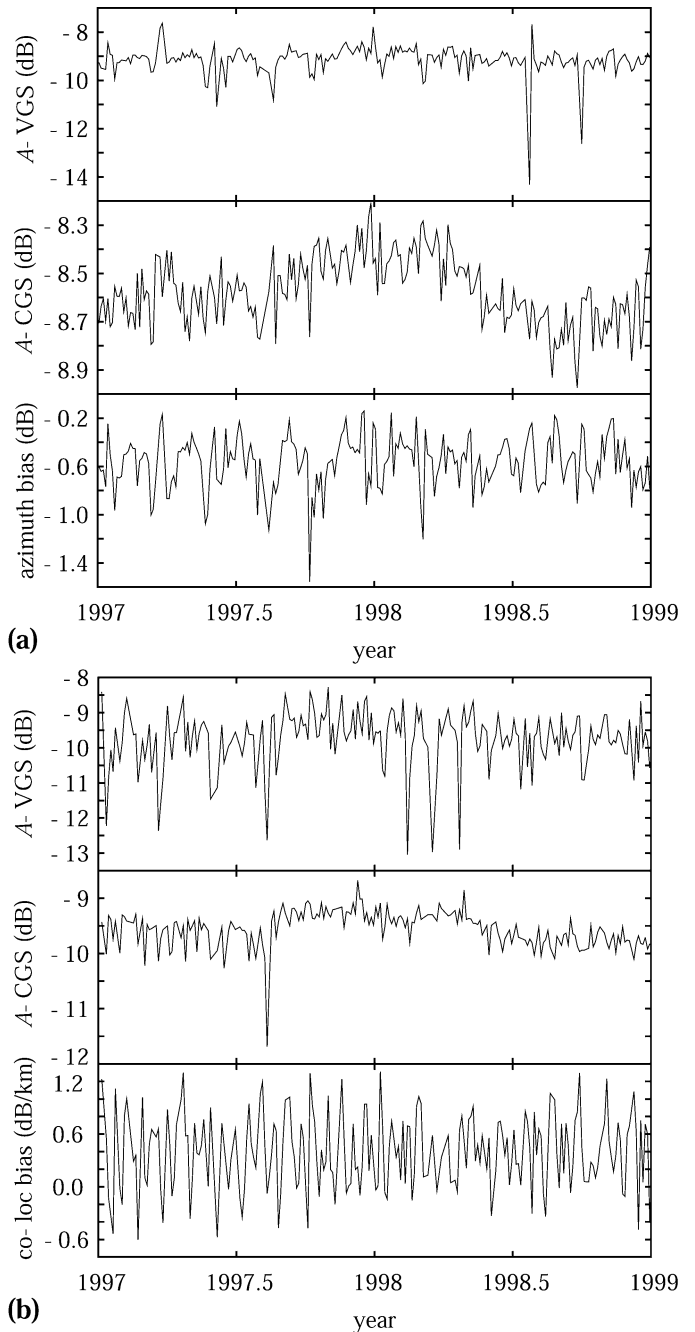


Fig. 14. Comparison of CGS A estimates and VGS A estimates at two locations. (a) Location 1 (78.6 N, 35.5 W) is in an area significantly affected by azimuth modulation. The bottom plot for location 1 shows the estimated bias over time due only to azimuth sampling. (a) At Location 2 (69.1 N, 35.7 W), a small melt event is observed as a sharp drop in A -CGS, which is obscured by the noise in the VGS A estimates. Location 2 is in an area significantly affected by colocation bias. The bottom plot for location 2 shows the estimated bias over time due only to the spatial sampling of the measurements.

Both methods are used to estimate the temporal variation in the backscatter at two locations. The estimates are shown in Fig. 14. For both cases, the variance of the CGS estimates of A is much smaller than the variance of the VGS A estimates. At location 1, which is in the dry snow zone, there is a crest in the CGS A estimates around the beginning of 1998 that is obscured in the VGS A estimates due to noise. Location 1 is also in a region where the azimuth dependence of σ° is relatively

large. The bottom plot for location 1 shows the signal due only to changes in azimuth sampling, which has been removed from CGS A estimates in the center plot by including azimuth dependence in the full model.

Location 2 is in the upper percolation zone. During the summer of 1997, a short melt event occurred that is observed as an abrupt drop in A followed by a small increase in the average value of A . This melt signal is difficult to detect from the VGS A estimates due to the high variance. Note that although the CGS geometry signature estimates are from the six months of data centered around January 1, 1998, two years of A estimates are shown. Prior to the melt event during the summer of 1997, there is an increased variance in the CGS A estimates. This is attributed to fundamental changes in the geometry signature occurring with the melt. The CGS geometry signature model, which was estimated from data after this melt event, does not accurately model the geometry dependence prior to the melt. Notwithstanding this modeling error, the variance of the CGS A estimates is consistently smaller than that of the VGS A estimates, even prior to the melt.

At location 2, the spatial gradient is large. The bottom plot for location 2 shows an estimate of the variation in the signal due only to the collocation bias from the spatial sampling of the measurement locations. This signal has been removed from CGS A estimates by including the spatial gradient in the model of the microwave signature of the snow.

These examples show some of the advantages of using the CGS assumptions when applicable. A key improvement is the reduced variance in the signal and the removal of unrealistic spikes in the data. The reduced variance is attributed in part to the inclusion of the azimuth and spatial gradient dependencies in the model. Higher temporal resolution may be obtained by averaging the CGS $A(t_i)$ estimates over shorter time intervals at the cost of increased noise.

V. SUMMARY

The σ° of the Greenland ice sheet may be modeled at a given point in time over a small region as a function of incidence angle, azimuth angle, measurement location, and measurement time. The contribution of each modeled dependency to the overall accuracy of the model is largest for incidence angle, which, in general, is followed by measurement location, then azimuth dependence, and finally, measurement time. The measurement location dependence is most significant in the upper percolation facies. Azimuth dependence is most significant in the lower dry snow zone, tapering off in the upper percolation zone. The azimuth dependence is primarily second order and exhibits little dependence on incidence angle. The orientation of the azimuth dependence is correlated with wind patterns across the ice sheet.

We have given examples of two applications for the descriptive empirical model developed herein. First, changes in the model parameters are valuable for tracking interannual changes on the ice sheet. Observed trends include increases and decreases in the melt intensity and extent, as well as interannual variations in accumulation. Second, the model is applicable for analysis of short-term variation in the average backscatter. Combined with the constant geometry signature assumption,

the model enables the estimation of average backscatter with smaller variance and/or increased temporal resolution compared with methods employed in previous studies.

The model also has other applications. For SAR, a knowledge of the azimuth modulation properties of the Greenland ice sheet is critical for accurate studies. Without proper adjustment for azimuth dependence, effects of a change in azimuth angle in an intercomparison of SAR σ° may be misinterpreted as physical change. Additionally, uncompensated azimuth dependence may result in image corruption for wide angle SAR. Comparisons between *in situ* and SAR measurements could also be affected by azimuth biases.

Extensive studies of the Greenland ice sheet have been conducted using passive observations, e.g., [10], [29]–[32]. Scatterometer observations nicely compliment passive microwave sensor observations. The differences between passive and active observations can be exploited to yield an improved understanding of surface conditions, e.g., [16] and [33].

ACKNOWLEDGMENT

NSCAT and ERS scatterometer data were obtained from the Physical Oceanography Distributed Data Archive (PO.DAAC) at the Jet Propulsion Laboratory, Pasadena, CA. J. Box and D. Bromwich kindly provided Greenland wind model data for our use. The authors thank the reviewers for their helpful comments and suggestions. This work was completed at the Brigham Young University Microwave Earth Remote Sensing Laboratory.

REFERENCES

- [1] W. S. B. Paterson and N. Reeh, "Thinning of the ice sheet in northeast Greenland over the past forty years," *Nature*, vol. 414, pp. 60–61, Nov. 2001.
- [2] D. G. Long and M. R. Drinkwater, "Greenland ice-sheet surface properties observed by the Seasat-A scatterometer at enhanced resolution," *J. Glaciol.*, vol. 40, no. 135, pp. 213–230, 1994.
- [3] V. Wismann, D. P. Winebrenner, K. Boehnke, and R. J. Arhern, "Snow accumulation on Greenland estimated from ERS scatterometer data," in *Proc. IGARSS*, 1997, pp. 1823–1825.
- [4] M. R. Drinkwater, D. G. Long, and A. W. Bingham, "Greenland snow accumulation estimates from satellite radar scatterometer data," *J. Geophys. Res.*, vol. 106, no. D24, pp. 33 935–33 950, Dec. 2001.
- [5] J. Munk, K. Jezek, and R. Forster, "An accumulation map for the greenland dry-snow zone derived from spaceborne radar," *J. Geophys. Res.*, vol. 108, no. D9, pp. 4280–4291, 2003.
- [6] V. Wismann, "Monitoring of seasonal snowmelt on Greenland with ERS scatterometer data," *IEEE Trans. Geosci. Remote Sens.*, vol. 38, no. 4, pp. 1821–1826, Jul. 2000.
- [7] I. S. Ashcraft and D. G. Long, "SeaWinds views Greenland," in *Proc. IGARSS*, vol. 3, 2000, pp. 1131–1136.
- [8] C. S. Benson, "Stratigraphic studies in the snow and firm of the Greenland ice sheet," *SIPRE Res. Rep.*, 1962.
- [9] K. Steffen, J. E. Box, and W. Abdalati, "Greenland climate network: GC-net," in *CRREL Special Report on Glaciers, Ice Sheets and Volcanoes*. Lansing, MI: CRREL, 1996, vol. 96–27, pp. 98–103.
- [10] W. Abdalati and K. Steffen, "Snowmelt on the Greenland ice sheet as derived from passive microwave satellite data," *J. Clim.*, vol. 10, pp. 165–175, Feb. 1997.
- [11] M. Fahnestock, R. Bindshadler, R. Kwok, and K. Jezek, "Greenland ice sheet surface properties and ice dynamics from ERS-1 SAR imagery," *Science*, vol. 262, pp. 1530–1534, Dec. 1993.
- [12] K. C. Jezek, M. R. Drinkwater, J. P. Crawford, R. Bindshadler, and R. Kwok, "Analysis of synthetic aperture radar data collected over the southwestern Greenland ice sheet," *J. Glaciol.*, vol. 39, no. 131, 1993.
- [13] K. C. Jezek, P. Gogineni, and M. Shanableh, "Radar measurements of melt zones on the Greenland ice sheet," *Geophys. Res. Lett.*, vol. 21, no. 1, pp. 33–36, Jan. 1994.

- [14] K. C. Partington, "Discrimination of glacier facies using multi-temporal SAR data," *J. Glaciol.*, vol. 44, no. 146, pp. 42–53, 1998.
- [15] F. Baumgartner, J. Munk, K. Jezek, and S. Gogineni, "On reconciling ground-based with space-borne normalized radar cross-section measurements," *IEEE Trans. Geosci. Remote Sens.*, vol. 40, no. 2, pp. 494–496, Feb. 2002.
- [16] D. G. Long and M. R. Drinkwater, "Azimuth variation in microwave scatterometer and radiometer data over Antarctica," *IEEE Trans. Geosci. Remote Sens.*, vol. 38, no. 4, pp. 1857–1870, Jul. 2000.
- [17] D. H. Bromwich, T. R. Parish, and C. A. Zorman, "The confluence zone of the intense katabatic winds at Terra Nova Bay, Antarctica, as derived from airborne sastrugi surveys and mesoscale numerical modeling," *J. Geophys. Res.*, vol. 95, no. D5, pp. 5495–5509, Apr. 1990.
- [18] I. S. Ashcraft and D. G. Long, "Relating microwave backscatter azimuth modulation to surface properties of the Greenland ice sheet, 2004." In Press.
- [19] M. Ledroit, F. Remy, and J. F. Minster, "Observations of the Antarctica ice sheet with the Seasat scatterometer: Relation to katabatic-wind intensity and direction," *J. Glaciol.*, vol. 39, no. 132, pp. 385–396, 1993.
- [20] N. Young, D. Hall, and G. Hyland, "Directional anisotropy of C-band backscatter and orientation of surface microrelief in East Antarctica," in *Proc. 1st Australian ERS Symp.*, Feb. 1996, pp. 117–126.
- [21] R. C. Bales, J. R. McConnell, E. Mosley-Thompson, and B. Csatho, "Accumulation over the Greenland ice sheet from historical and recent records," *J. Geophys. Res.*, vol. 106, no. D24, pp. 33 813–33 825, Dec. 2001.
- [22] D. H. Bromwich, Y. Du, and K. M. Hines, "Wintertime surface winds over the Greenland ice sheet," *Mon. Weather Rev.*, vol. 124, pp. 1941–1947, Sep. 1996.
- [23] J. E. Box, D. H. Bromwich, and L.-S. Bai, "Greenland ice sheet surface mass balance 1991–2000: Application of polar MM5 mesoscale model and in situ data," *J. Geophys. Res.*, vol. 109, no. D16, Aug. 2004.
- [24] I. S. Ashcraft and D. G. Long, "SeaWinds views Greenland," in *Proc. IGARSS*, vol. 3, 2000, pp. 1131–1136.
- [25] J. D. Pack, J. W. Wallace, and M. A. Jensen, "Greenland snow ablation and accumulation observed using ERS and SSM/I data," in *Proc. IGARSS*, 2000, pp. 1128–1130.
- [26] J. R. McConnell, G. Lamorey, E. Hanna, E. Mosley-Thompson, R. C. Bales, D. Belle-Oudry, and J. D. Kyne, "Annual net snow accumulation over southern Greenland from 1975 to 1998," *J. Geophys. Res.*, vol. 106, no. D24, pp. 33 827–33 837, Dec. 2001.
- [27] M. R. Drinkwater and D. G. Long, *Seasat, ERS-1/2 and NSCAT Scatterometer Observed Changes on the Large Ice Sheets*, Noordwijk, The Netherlands: ESA ESTEC, Nov. 1998, pp. 91–96.
- [28] A. W. Bingham and M. R. Drinkwater, "Recent changes in the microwave scattering properties of the Antarctic ice sheet," *IEEE Trans. Geosci. Remote Sens.*, vol. 38, no. 4, pp. 1810–1820, Jul. 2000.
- [29] W. Abdalati and K. Steffen, "Passive microwave-derived snow melt regions on the Greenland ice sheet," *Geophys. Res. Lett.*, vol. 22, no. 7, pp. 787–790, Apr. 1995.
- [30] T. L. Mote and M. R. Anderson, "Variations in snowpack melt on the Greenland ice sheet based on passive-microwave measurements," *J. Glaciol.*, vol. 41, no. 137, pp. 51–60, 1995.
- [31] J. F. Bolzan and K. C. Jezek, "Accumulation rate changes in central Greenland from passive microwave data," *Polar Geogr.*, vol. 24, no. 2, pp. 98–112, 2000.
- [32] M. Joshi, C. Merry, K. Jezek, and J. Bolzan, "An edge detection technique to estimate melt duration, season and melt extent on the Greenland ice sheet using passive microwave data," *Geophys. Res. Lett.*, vol. 28, no. 18, pp. 3497–3500, 2001.
- [33] J. D. Pack and M. A. Jensen, "Estimating snow accumulation on Greenland from SSM/I radiometer data," in *Proc. IGARSS*, 2001, pp. 946–948.

Ivan S. Ashcraft received the Ph.D. degree in electrical engineering from Brigham Young University (BYU), Provo, UT, in 2004.

At BYU, he worked with the BYU Center for Remote Sensing focusing on applications of microwave remote sensing for monitoring the effects of climate change on the Greenland Ice Sheet. He is currently with BYU, Rexburg, ID.



David G. Long (S'80–SM'98) received the Ph.D. degree in electrical engineering from the University of Southern California, Los Angeles, in 1989.

From 1983 to 1990, he was with the National Aeronautics and Space Administration (NASA) Jet Propulsion Laboratory (JPL), Pasadena, CA, where he developed advanced radar remote sensing systems. While at JPL, he was the Senior Project Engineer on the NASA Scatterometer (NSCAT) project, which was flown aboard the Japanese Advanced Earth Observing System (ADEOS) from 1996 to 1997. He was also the Experiment Manager and Project Engineer for the SCANSAT scatterometer (now known as SeaWinds). In 1990, he joined the Department of Electrical and Computer Engineering, Brigham Young University (BYU), Provo, UT, where he currently teaches upper division and graduate courses in communications, microwave remote sensing, radar, and signal processing, is the Director of BYU's Center for Remote Sensing, and is the Head of the Microwave Earth Remote Sensing Laboratory. He is the Principal Investigator on several NASA-sponsored interdisciplinary research projects in microwave remote sensing and innovative radar systems. He has numerous publications in signal processing and radar scatterometry. His research interests include microwave remote sensing, radar, polar ice, signal processing, estimation theory, and mesoscale atmospheric dynamics. He has over 250 publications in the open literature.

Dr. Long has received the NASA Certificate of Recognition several times. He is an Associate Editor for the IEEE GEOSCIENCE AND REMOTE SENSING LETTERS.